EPITAXIAL FILMS

Kinetic acceleration of MoS_2 growth by oxy-metal-organic chemical vapor deposition

Lei Liu[1]†, Yushu Wang[1]†, Ruikang Dong[1]†, Dongxu Fan[1,2,3]†, Si Meng[1], Lang Wu[1,2], Shengqiang Wu[1], Wei Xu[1], Mingwei Feng[1,2], Ningmu Zou[1,2], Qingyu Yan[4], Zehua Hu[4], Fei Lu[4], Shitong Zhu[5], Yuan Gao[4], Liang Ma[1,6], Yi Shi[4], Taotao Li[1,2,3]*, Jinlan Wang[1,6]*, Xinran Wang[1,2,3,4]*

Kinetics determine the growth behavior of thin films, particularly for atomically thin transition-metal dichalcogenides. Metal-organic (MO) chemical vapor deposition (CVD) offers promise for scalable growth, but the reactions are kinetically limited, leading to nanometer-scale domain size and carbon contaminations. Here, we unveil the fundamental kinetic limitations and overcome them by introducing oxygen-assisted MOCVD (oxy-MOCVD) technology. By tuning reactions with oxygen, MO precursors are converted into high-purity transition-metal oxides and chalcogens, producing aligned molybdenum disulfide (MoS_2) domains with a size and growth rate that are orders of magnitude larger than conventional MOCVD. The MoS_2 is free of carbon impurities and exhibits average mobility exceeding 100 square centimeters per volt per second. The scalability of oxy-MOCVD is demonstrated by 150-millimeter single-crystal MoS_2 wafers, proving the feasibility of industrial-scale production.

Thin-film growth is inherently a nonequilibrium process governed by the interplay between thermodynamics and kinetics (*1*–*3*). Growth kinetics play a central role in determining thin film nucleation behavior, domain evolution, and quality. This is particularly relevant for atomically thin two-dimensional (2D) semiconductors because of the relatively weak thermodynamic driving force by substrate van der Waals interactions. The growth kinetics of transition metal dichalcogenides (TMDCs) typically involve sublimation of precursors into the gas phase, sulfurization of transition metal–containing species, and subsequent surface growth (*4*–*6*). Despite notable progress in TMDC growth, the fundamental kinetics behind these processes remain poorly understood and pose challenges for the transition from academic laboratories to industry (*7*–*10*).

Compared with solid-source chemical vapor diffusion (CVD), gaseous-source metal-organic (MO) CVD (MOCVD) offers precise control of precursor delivery and large-area uniformity, enabling the production of TMDC films up to 200 mm in diameter (*11*–*18*). However, MOCVD often results in small domain sizes, high grain boundary densities, and inevitable carbon contamination. This is due to the chemical decomposition of MO precursors into zero-valent metal, which has low vapor pressure and limited adatom mobility compared with metal oxides (*5*). On the chalcogen side, hydride precursors suffer from slow growth because of high activation barriers for hydrogen removal, whereas organo-chalcogen precursors offer better volatility but introduce carbonaceous by-products during pyrolysis (*19*–*22*). These results underscore the critical influence of precursor chemistry on growth behavior. A deeper understanding and modulation of reaction kinetics are urgently needed to guide precursor design, optimize growth pathways, and improve film quality for industrial-scale TMDC production.

Recently, we reported epitaxial growth of 150-mm single-crystalline TMDC wafers on lanthanum-passivated C-plane sapphire (*23*). A single atomic layer of lanthanum reduced the surface symmetry and increased the energy difference between antiparallel domains, leading to unidirectional domain alignment. Although high domain alignment was achieved, the domain sizes remain at the nanometer scale for the MOCVD process, which could introduce more defects during domain merging.

In this work, we focused on the role of reaction kinetics in improving domain size, growth rate, and film quality. We elucidated the fundamental kinetic bottlenecks limiting the growth of high-quality MoS_2 and introduced a new technology, oxygen-assisted MOCVD (oxy-MOCVD), to overcome them. By precisely introducing oxygen to prereact with molybdenum hexacarbonyl [$Mo(CO)_6$] and carbon disulfide (CS_2), we generated high-purity molybdenum trioxide (MoO_3) and sulfur as reactive intermediates. These intermediates enabled the growth of unidirectionally aligned molybdenum disulfide (MoS_2) domains on sapphire substrates, with larger domain sizes (hundreds of micrometers) and growth rates exceeding conventional MOCVD by more than two orders of magnitude while maintaining wafer-scale uniformity.

The resulting MoS_2 films are free of carbon impurities and exhibit room-temperature carrier mobilities of up to 122.9 $cm^2\ V^{-1}\ s^{-1}$, with an average of 101.3 $cm^2\ V^{-1}\ s^{-1}$, which are comparable to the best reported CVD-grown films. Furthermore, we demonstrated the scalability of oxy-MOCVD by synthesizing uniform 150-mm single-crystalline MoS_2 wafers. By precisely controlling reaction kinetics, this approach bridges the gap between lab-scale CVD quality and industrial-scale MOCVD scalability.

Growth kinetics of MoS_2 in MOCVD

Although hydrogen sulfide (H_2S) and organo-chalcogen compounds are conventional sulfur sources in MOCVD, we introduce CS_2 for the first time as a precursor for TMDC films. Its hydrogen-free nature and low carbon content present a superior alternative for this application (see the supplementary text). To determine the limitations of conventional MOCVD, we first performed theoretical investigations of MoS_2 growth kinetics using $Mo(CO)_6$ as the molybdenum source and H_2S or CS_2 as the sulfur source (Fig. 1A) (*11*). The analysis was performed based on ab initio molecular dynamics simulations and density functional theory calculations (see the materials and methods). Prior theoretical studies and our simulations have shown that $Mo(CO)_6$ rapidly dissociates into $Mo(CO)_3$ before reacting with sulfur precursors (*19*, *24*) (the first step shown in fig. S1A). Therefore, we used $Mo(CO)_3$ as the starting point in all reactions.

Reaction I [$H_2S + Mo(CO)_6 \rightarrow MoS_4H_2 + CO + H_2$; fig. S1A and movie S1] is the most widely adopted MOCVD process. The H_2S-driven sulfurization of $Mo(CO)_3$ gradually replaces the remaining three CO ligands. Redundant hydrogen atoms spontaneously dimerize and desorb from the cluster as H_2 molecules, resulting in a stable MoS_4H_2 monomer. The reaction is exothermic, with a reaction enthalpy (ΔH) of –1.24 eV, but the rate-limiting step has a significant energy barrier of 2.02 eV, suggesting very slow kinetics, in agreement with previous reports and our own experiments (*19*).

In reaction II [$CS_2 + Mo(CO)_6 \rightarrow MoS_5C + CO + C_3S_2$; fig. S1A and movie S2], we used CS_2 as the sulfur precursor, considering its lower toxicity, suitable volatility, and nonalkyl nature, which helps to reduce carbon contamination. Our calculations showed that CS_2 can react with $Mo(CO)_3$, but carbon desorption from the cluster is energetically unfavorable. Instead, the carbon atoms gradually aggregate into

[1]Suzhou Laboratory, Suzhou, China. [2]School of Integrated Circuits, Nanjing University, Suzhou, China. [3]Interdisciplinary Research Center for Future Intelligent Chips (Chip-X), Nanjing University, Suzhou, China. [4]National Laboratory of Solid State Microstructures, School of Electronic Science and Engineering and Collaborative Innovation Center of Advanced Microstructures, Nanjing University, Nanjing, China. [5]Nanjing Extremo Technology Co., Ltd., Nanjing, China. [6]Key Laboratory of Quantum Materials and Devices of Ministry of Education, School of Physics, Southeast University, Nanjing, China. ***Corresponding author. Email: ttli@nju.edu.cn (T.L.); jlwang@seu.edu.cn (J.W.); xrwang@nju.edu.cn or wangxr@szlab.ac.cn (X.W.)** †These authors contributed equally to this work.

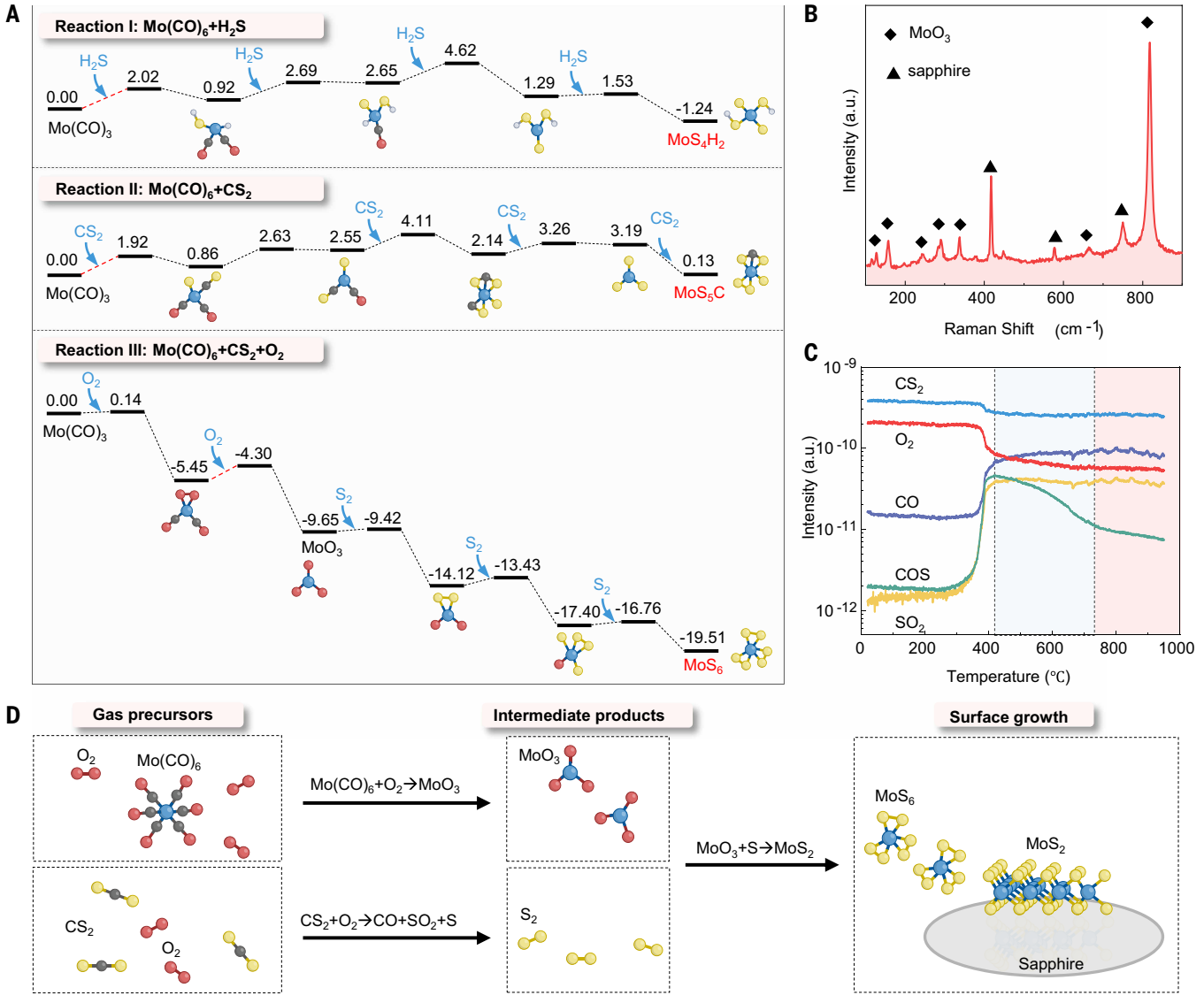

Fig. 1. Growth kinetics of MoS_2 by oxy-MOCVD and conventional MOCVD. (**A**) Three reactions corresponding to different precursor combinations. Red lines represent reaction steps of the largest energy barrier. (**B**) Raman spectra of MoO_3 after oxidation of $Mo(CO)_6$ at 400°C. (**C**) In situ mass spectrometry analysis of the intermediate species from the reaction of CS_2 and O_2. (**D**) Illustration of the complete reaction process of oxy-MOCVD. a.u., arbitrary units.

chain-like structures and desorb as carbon-sulfur hybrids, forming MoS_5C monomers. The reaction is endothermic, with ΔH = 0.13 eV, and the energy barrier of 1.92 eV is still relatively high, although slightly lower than that of reaction I. In addition, the carbonaceous product indicates that this reaction could introduce carbon impurities, as confirmed by our experiment in the next section.

The above analyses pinpoint two critical kinetics challenges in TMDC growth by conventional MOCVD: significant energy barriers in precursor sulfurization and carbon impurities in the intermediates. To address these challenges, we introduced oxygen into the reactions and propose an oxy-MOCVD strategy [reaction III, $CS_2 + Mo(CO)_6 + O_2 \rightarrow MoS_6 + CO + COS + CO_2$; fig. S1A and movie S3]. Along this path, $Mo(CO)_3$ is first oxidized by O_2 to MoO_3, a highly exothermic process (ΔH = –9.65 eV) that involves a small energy barrier of 1.15 eV. We attributed this facilitated reactivity to the oxygen-assisted desorption of CO ligands. Concurrently, O_2 oxidizes CS_2 to yield elemental sulfur (figs. S1B and S3A), which then sulfurizes the MoO_3, producing a hydrogen- and carbon-free MoS_6 monomer. The entire oxy-MOCVD reaction is exothermic, with ΔH = –19.51 eV, which is more than one order of magnitude larger than conventional MOCVD without oxygen. Finally, the MoS_6 monomers serve as the primary precursor species for the epitaxial growth of MoS_2 on the substrate (*6*, *19*, *24*, *25*). Furthermore, the edge adsorption dynamics of the three pathways were theoretically investigated. As illustrated in fig. S2, MoS_6 exhibits a lower edge adsorption energy compared with MoS_4H_2 and MoS_5C. This indicates that the introduction of oxygen not only accelerates the reaction kinetics but also enhances the edge adsorption by suppressing hydrogen or carbon atom incorporation, enabling the growth of large-area, high-quality MoS_2.

We experimentally validated the calculated reaction pathway of oxy-MOCVD. On the transition-metal side, we found that $Mo(CO)_6$ reacts with O_2 to form MoO_3 at temperatures above 400°C (Fig. 1B and fig. S3B). On the chalcogen side, we performed in situ mass spectrometry to detect the intermediate sulfur species during prereaction of CS_2 and O_2 (Fig. 1C). The reaction initiated at ~375°C, where we observed a decrease of CS_2 and O_2 concentration and simultaneous formation of several products, including CO, sulfur dioxide (SO_2), carbonyl sulfide (COS), and elemental sulfur. The formation of abundant elemental sulfur was visible at the unheated tube region near the gas outlet (fig. S3C). The reaction can be described as reaction IV: $CS_2 + O_2 \rightarrow COS + CO + SO_2 + S$.

Figure 1C shows that COS can be further oxidized at high temperatures. At the temperature of MoS_2 growth (~950°C), COS is almost completely consumed. Because SO_2 does not react with MoO_3, elemental sulfur was the primary contributor to the sulfur source. These experimental results were fully consistent with the calculations in Fig. 1A and demonstrated the feasibility of oxy-MOCVD. In our oxy-MOCVD process, O_2 should be precisely dosed to maintain overall growth along the desired reaction pathway (see the supplementary text). The complete oxy-MOCVD reaction process is illustrated in Fig. 1D.

Oxy-MOCVD growth of MoS_2

Guided by the process outlined in Fig. 1, we grew MoS_2 using oxy-MOCVD in a custom-designed hot-wall MOCVD system (ExtreMO D200 Ultra) with prereaction chambers to mix MO precursors with oxygen in a precisely controlled manner (see the materials and methods and fig. S4). The growth substrate was C-plane sapphire with a miscut angle of 1° toward the A-axis (C/A-1°) (*8*). To achieve high-quality MoS_2 growth, the process was maintained within the diffusion-limited regime (see the supplementary text and fig. S5). Precise control of oxygen flow ensures high material quality (see the supplementary text and fig. S6). We also conducted control MOCVD experiments using H_2S (H_2S-MOCVD) and CS_2 (CS_2-MOCVD) as sulfur precursors without oxygen in the same system.

Figure 2A presents an optical microscopy (OM) image of a monolayer MoS_2 domain grown by oxy-MOCVD, with a lateral size of ~260 μm. More OM images in fig. S7 showed grain sizes up to several hundred micrometers. By contrast, MoS_2 grown by CS_2-MOCVD and H_2S-MOCVD exhibited typical grain sizes of ~100 and ~30 nm, respectively (Fig. 2, B and C), consistent with previous reports (*20*). Because the growth time was identical for the three processes, these differences indicated that the growth rate of oxy-MOCVD was two to three orders of magnitude faster than conventional MOCVD as a result of the smaller energy barrier in the reaction pathway (Fig. 1A). On the basis of the OM and atomic force microscopy (AFM) images, we used a pixel-level machine learning classification artificial intelligence (AI) model to analyze the MoS_2 domain area from the three processes statistically (see the materials and methods). The average domain area of oxy-MOCVD MoS_2 was 2.58×10^3 μm^2, which was five to six orders of magnitude larger than that grown by CS_2-MOCVD (1.93×10^{-2} μm^2), H_2S-MOCVD (2.39×10^{-3} μm^2) (Fig. 2G), and H_2S-MOCVD on La-passivated sapphire (5.44×10^{-3} μm^2) (*23*).

Next, we examined the domain orientations of MoS_2. As shown in fig. S8, for oxy-MOCVD, triangular MoS_2 domains were unidirectionally aligned on the C/A-1° sapphire substrate in a R30° epitaxial relationship. This orientation was the same as CVD using MoO_3 and sulfur (*8*), as expected from the reaction pathway in Fig. 1. As a result, dark-field transmission electron microscopy (DF-TEM) of continuous film displays uniform contrast and a single set of diffraction spots, confirming the single-crystalline nature (Fig. 2D). In addition, atomic-resolution STEM images reveal the crystalline nature of MoS_2 with low density of defects (fig. S9). Growth results on C/A 8° and 15° sapphire further demonstrate the robustness of oxy-MOCVD with respect to miscut angle (fig. S10). The oxy-MOCVD is also compatible with our recently reported La-passivated sapphire substrate (*23*), on which unidirectional MoS_2 domains with a R0° epitaxial relationship were obtained (fig. S11). The domain area (76.6 μm^2) was increased by about four orders of magnitude compared with conventional MOCVD. The combination of substrate engineering and kinetic control forms the basis for robust production of high-quality single-crystal 2D semiconductors.

By contrast, the MOCVD films were polycrystalline with both R0° and R30° epitaxial relations, as shown by two sets of diffraction spots rotated by 30° (Fig. 2, E and F; yellow/orange indicates R0° and blue/green indicates R30°). Each epitaxial relation consists of two antiparallel directions rotated by 180°. A small fraction of domains corresponding to the rings in diffraction patterns exhibited other epitaxial relations, as denoted by the gray color. The coexistence of different domain orientations resulted in multiple types of grain boundaries, including mirror twin boundaries and dislocation cores such as 5- and 7-membered rings defects (*26*). These structural defects intrinsic to the MOCVD films severely degraded their electrical and mechanical properties.

In addition, pyrolysis of organo-chalcogens (*16*) leads to carbon impurities in MOCVD MoS_2. We examined the carbon impurity level in the MoS_2 samples using C 1s core-level x-ray photoemission spectroscopy (XPS) (Fig. 2H). We observed a strong C 1s peak in CS_2-MOCVD MoS_2 (Fig. 1A), but for oxy-MOCVD, no C 1s peak was observed. Carbon contamination was effectively eliminated by introducing oxygen, which completely oxidized the $Mo(CO)_6$ and CS_2 precursors to MoO_3 and sulfur.

The high quality of oxy-MOCVD MoS_2 was further supported by prominent photoluminescence (PL) centered at the neutral exciton (1.87 eV), the intensity of which was ~20 and ~900 times higher

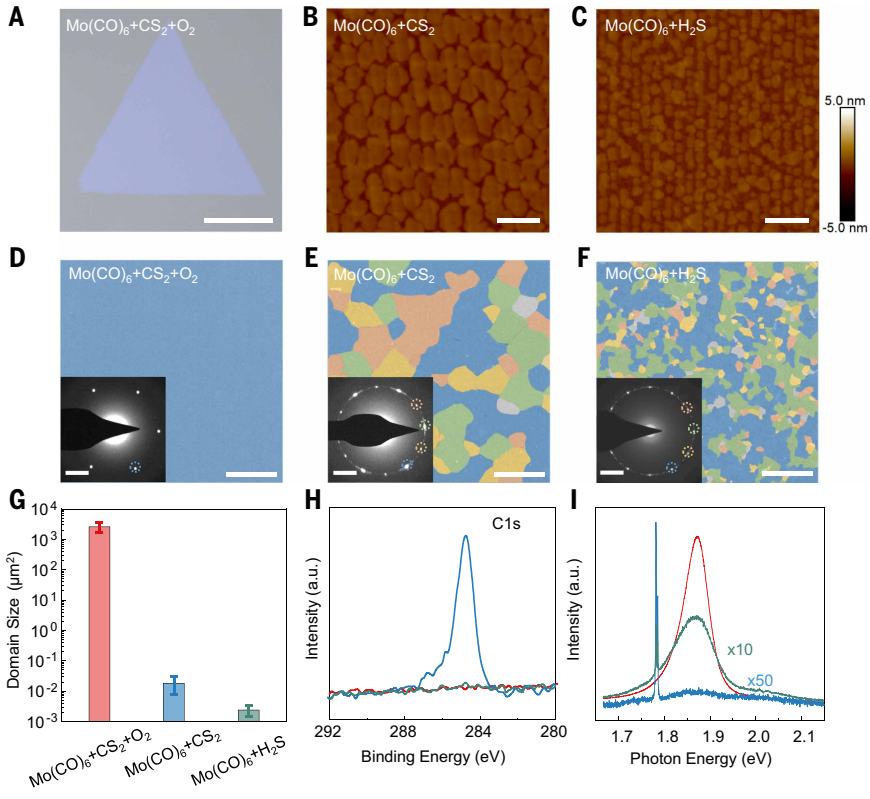

Fig. 2. Characterizations of MoS_2 grown by oxy-MOCVD and conventional MOCVD. (**A**) Optical microscopy image of a MoS_2 domain grown by oxy-MOCVD. Scale bar, 100 μm. (**B** and **C**) AFM images of the MoS_2 grown by CS_2-MOCVD and H_2S-MOCVD. Scale bar, 100 nm. (**D** to **F**) False-color DF-TEM images of MoS_2 film from oxy-MOCVD (D), CS_2-MOCVD (E), and H_2S-MOCVD (F). Areas with blue, yellow, green, and orange were created by selecting the diffraction spot marked in circles with the corresponding color. The gray areas are domains with other orientations. Yellow/orange and blue/green indicate antiparallel domains rotated by 180° in R0° and R30°. Scale bar, 500 nm. Insets are corresponding selected area electron diffraction (SAED) patterns. Scale bar, 2/nm. (**G** to **I**) Statistical analysis of the domain area (G) (error bars represent SD), the high-resolution spectrum of the C 1s core level (H), and the PL spectrum (I) of MoS_2 grown by the three reactions.

than that of H_2S-MOCVD and CS_2-MOCVD MoS_2, respectively. The bright PL indicates the absence of quenching centers such as carbon impurities and mirror twin boundaries (*20*, *26*). Cryogenic PL measurement at 4 K showed narrow neutral exciton emission with a full width at half maximum (FWHM) of 26.2 meV and a small trion composition indicative of low doping (fig. S12A). No defect-related emissions were detected. Compared with the mechanically exfoliated and CVD-grown MoS_2 from our laboratory, the oxy-MOCVD sample had a narrower exciton FWHM and reduced trion emission (fig. S12B).

Electrical properties of oxy-MOCVD MoS_2

To evaluate the electrical properties of oxy-MOCVD MoS_2, we fabricated field-effect transistor (FET) arrays with 50 μm channel length and Sb $(01\bar{1}2)$ ohmic contacts (Fig. 3 and see the materials and methods) (*27*). Figure 3A displays the OM image of the FET array, where each die contains 45 unit cells and 180 FET devices. The I_d-V_{gs} transfer characteristics of 540 FETs are presented in Fig. 3B, showing enhanced-mode n-type behavior with very small variations. The on-state current of our oxy-MOCVD MoS_2 was one to two orders of magnitude higher than the MOCVD counterparts. The field-effect mobility is calculated by $\mu = \frac{g_m}{C_g V_{ds}} \cdot \frac{L_{ch}}{W_{ch}}$, where $C_g = 6.67 \times 10^{-8}$ F cm^{-2} is the gate capacitance, g_m is the transconductance, and W_{ch} and L_{ch} are the channel width and length, respectively. The oxy-MOCVD MoS_2 showed $\mu = 101.3 \pm 9.5$ cm^2 V^{-1} s^{-1} with maximum $\mu = 122.9$ cm^2 V^{-1} s^{-1}. The average mobility was >10 and 50 times higher than that of CS_2-MOCVD MoS_2 (9.0 cm^2 V^{-1} s^{-1}) and H_2S-MOCVD MoS_2 (1.8 cm^2 V^{-1} s^{-1}), respectively (Fig. 3C). Moreover, oxy-MOCVD MoS_2 exhibited the lowest mobility variation of 9.3% (defined as the ratio of SD over mean value) (Fig. 3C). The MoS_2 showed phonon-limited rather than defect-limited transport at low temperatures. At 30 K, the mobility reached 679.7 cm^2 V^{-1} s^{-1}, indicating a low level of defects achieved by oxy-MOCVD (fig. S13).

Other than mobility, key electrical parameters, including max transconductance (g), on-state current (I_{on}), subthreshold swing (*SS*), threshold voltage (V_{th}), and current on/off ratio (I_{on}/I_{off}), were also systematically extracted (Fig. 3E). Corresponding data are shown in table S1. Statistical analysis indicates that the oxy-MOCVD MoS_2 exhibited higher performance and uniformity across all metrics than CS_2-MOCVD and H_2S-MOCVD. Notably, the smaller *SS*, V_{th}, and large I_{on}/I_{off} up to 10^9 are all indicative of reduced defect and trap density compared with MOCVD samples. Our devices currently use a dielectric layer that is relatively thick and has a material with a low dielectric constant (low-κ). This combination results in a small C_g, thereby significantly increasing the overall *SS* value. Replacing the low-κ dielectric with a high-κ material and reducing its thickness are the most promising strategies for substantially improving *SS* in subsequent optimizations.

We further benchmarked the electrical performance with MOCVD MoS_2 in the literature (*11*, *15*, *17*, *18*, *28*–*33*). In Fig. 3D, our oxy-MOCVD MoS_2 stands out in the upper right corner, achieving the highest mobility and I_{on}/I_{off} reported to date in MOCVD. Moreover, our material outperforms even the state-of-the-art CVD-grown samples reported in the literature (*8*), as evidenced by its superior threshold voltage and mobility, which attest to its superior quality. Previously, the highest mobility for MOCVD MoS_2 was 47 cm^2 V^{-1} s^{-1}, synthesized using $Mo(CO)_6$ and H_2S precursors at 1000°C (*29*). The substantial improvement in electrical and optical properties underscores the critical role of reaction chemistry and kinetics in optimizing the quality of TMDCs toward the intrinsic limit. Systematic comparison with conventional MOCVD is presented in table S2, clearly demonstrating the overwhelming advantage of oxy-MOCVD.

Single-crystalline 150-mm MoS_2

To demonstrate the scalability of oxy-MOCVD for industrial production, we grew highly uniform single-crystalline MoS_2 on a 150-mm C/A sapphire substrate (the largest substrate size available to us) (Fig. 4). Before merging into a continuous film, unidirectionally aligned triangular MoS_2 domains were observed (Fig. 4A and fig. S14). Growth results from multiple runs showed excellent reproducibility and potential for large-scale industrial deployment (fig. S15). The percentage of unidirectional alignment reached nearly 100% across the entire 150-mm wafer analyzed by the AI model (movie S4). Figure 4B shows a photograph of the 150-mm single-crystalline MoS_2 wafer with excellent homogeneity. OM images of the continuous film revealed the uniform thickness across the wafer (fig. S16). Multiple submillimeter-scale second-harmonic generation (SHG) mappings revealed uniform intensity with no clear signs of grain boundaries (fig. S17).

We further performed Raman, PL, and SHG mappings on the entire MoS_2 wafer (see the materials and methods). As shown in Fig. 4, C to E, all three mappings exhibited excellent wafer-scale uniformity. Quantitative spatial characterizations revealed unprecedented material consistency: Raman mapping showed a narrow distribution of the separation of the E^1_{2g} and A_{1g} peaks (18.5 ± 0.23 cm^{-1}), validating the uniform monolayer thickness (Fig. 4C and fig. S18A). PL mapping showed an intensity variation of <9% across the wafer (Fig. 4D and fig. S18B). SHG mapping demonstrated uniform color contrast, verifying the single-crystalline nature (Fig. 4E and fig. S18C). Raman and PL line scans across the 150-mm-diameter sample also demonstrated the large-area uniformity (Fig. 4, F and G). From these wafer-scale characterizations, we conclude that our oxy-MOCVD achieves exceptional material quality and uniformity.

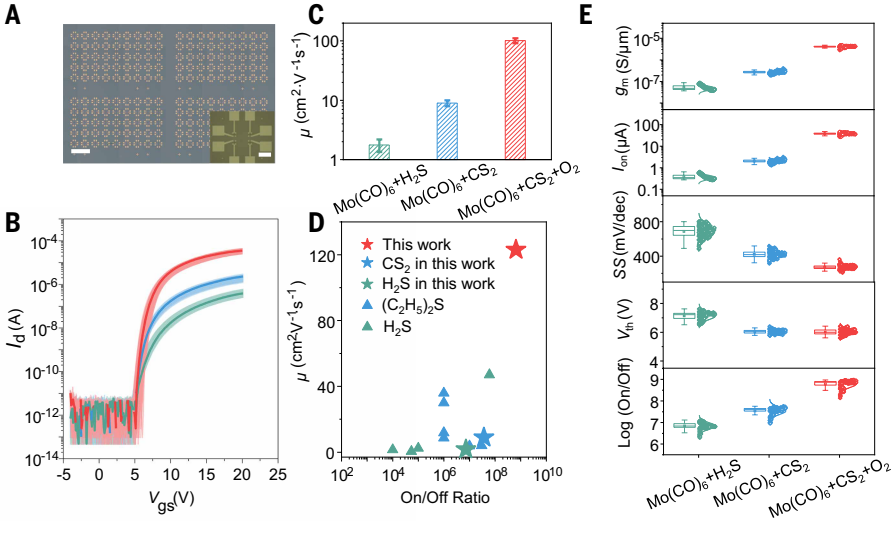

Fig. 3. Electrical performance of MoS_2. (**A**) OM image of a FET array fabricated on Al_2O_3/Si substrate. Scale bar, 0.6 mm. Inset is an enlarged image of a unit cell consisting of four FETs. Scale bar, 60 μm. (**B**) I_d-V_{gs} characteristics of MoS_2 FETs at V_{ds} = 1.5 V. Devices are grouped by the precursor used for MoS_2 growth: $Mo(CO)_6 + CS_2 + O_2$ (red, 200 FETs), $Mo(CO)_6 + CS_2$ (blue, 170 FETs), and $Mo(CO)_6 + H_2S$ (green, 170 FETs). (**C**) Mobility comparisons. Column heights represent the mean field effect mobility (μ) and error bars indicate the SD (σ). (**D**) Benchmark of the maximum μ versus I_{on}/I_{off}. (**E**) Comparison of key FET parameters: boxplot statistics and Gaussian fitting of V_{th}, *SS*, μ, I_{on}, and log(I_{on}/I_{off}).

Conclusions

We developed an oxy-MOCVD technology that enables the synthesis of 150-mm high-quality single-crystalline MoS_2 wafers. By carefully analyzing growth kinetics and introducing oxygen into

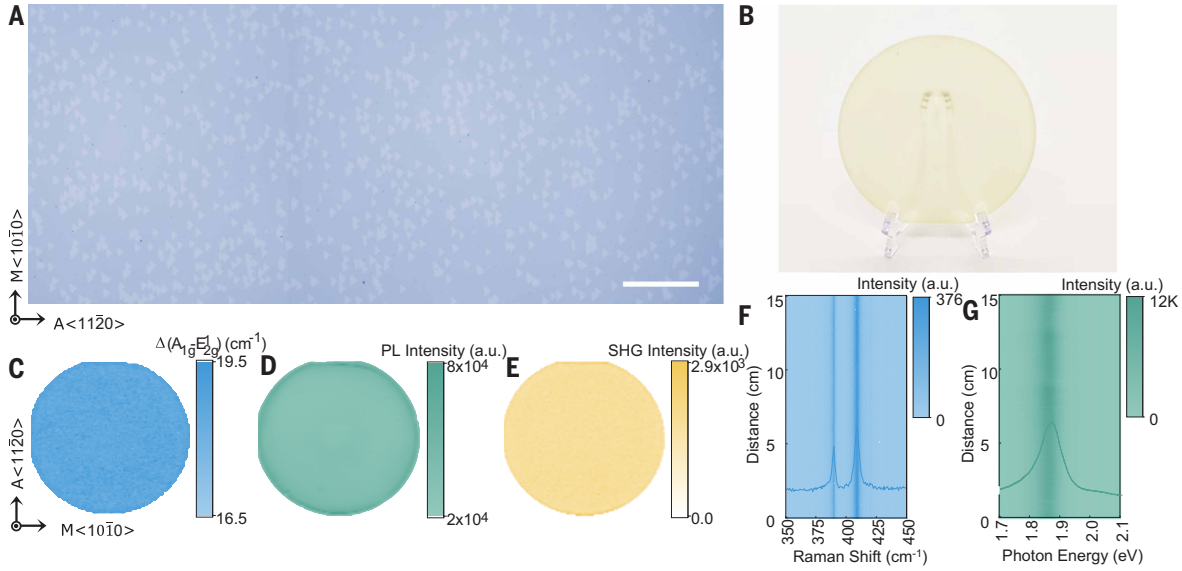

Fig. 4. Uniformity characterization of 6-inch single-crystalline MoS_2 wafer. (**A**) OM image of unidirectional MoS_2 flakes. Scale bar, 100 μm. (**B**) Photograph of the 150-mm monolayer MoS_2 wafer grown on a c/a-1° sapphire substrate. (**C** to **E**) Mapping of Raman peak position difference $\Delta(A_{1g} - E^1_{2g})$ (C), PL intensity (D), and SHG intensity (E) over a 150-mm MoS_2 wafer. (**F** and **G**) Line scan mapping of Raman (F) and PL (G) along 150-mm wafer diameter. Insets are the corresponding spectra.

prereactions with MO precursors, our approach achieved unidirectionally aligned, carbon-contamination-free MoS_2 with the best electrical performance, far surpassing the limitations of conventional MOCVD. This work not only sheds light on the critical role of growth kinetics but also establishes a technological breakthrough toward industrial-scale production of 2D semiconductors.

REFERENCES AND NOTES

1. Z. Zhang, M. G. Lagally, *Science* **276**, 377–383 (1997).
2. R. P. Parikh *et al.*, *J. Cryst. Growth* **296**, 15–26 (2006).
3. S. Nakamura, Y. Harada, M. Seno, *Appl. Phys. Lett.* **58**, 2021–2023 (1991).
4. J. Dong, L. Zhang, F. Ding, *Adv. Mater.* **31**, e1801583 (2019).
5. X. Zhang *et al.*, *Nat. Rev. Methods Primers* **5**, 57 (2025).
6. J. Lei, Y. Xie, B. I. Yakobson, *ACS Nano* **15**, 10525–10531 (2021).
7. H. Qiu *et al.*, *Sci. China Inf. Sci.* **67**, 160400 (2024).
8. T. Li *et al.*, *Nat. Nanotechnol.* **16**, 1201–1207 (2021).
9. J. H. Fu *et al.*, *Nat. Nanotechnol.* **18**, 1289–1294 (2023).
10. H. Jiang *et al.*, *Nat. Mater.* **24**, 188–196 (2025).
11. K. Kang *et al.*, *Nature* **520**, 656–660 (2015).
12. A. T. Hoang *et al.*, *Nat. Nanotechnol.* **18**, 1439–1447 (2023).
13. H. Zhu *et al.*, *Nat. Nanotechnol.* **18**, 1295–1302 (2023).
14. X. Zhang *et al.*, *Nano Lett.* **18**, 1049–1056 (2018).
15. M. Seol *et al.*, *Adv. Mater.* **32**, e2003542 (2020).
16. T. Zhang, J. Wang, P. Wu, A.-Y. Lu, J. Kong, *Nat. Rev. Mater.* **8**, 799–821 (2023).
17. J. Zhu *et al.*, *Nat. Nanotechnol.* **18**, 456–463 (2023).
18. T. Kim *et al.*, *Nanotechnology* **28**, 18LT01 (2017).
19. S. Ghorai, A. Govind Rajan, *Chem. Mater.* **36**, 2698–2710 (2024).
20. C. M. Schaefer *et al.*, *Chem. Mater.* **33**, 4474–4487 (2021).
21. X. Zhang *et al.*, *J. Electron. Mater.* **45**, 6273–6279 (2016).
22. T. H. Choudhury *et al.*, *Cryst. Growth Des.* **18**, 4357–4364 (2018).
23. X. Zou *et al.*, *Science* **390**, eaea0849 (2025).
24. M. Yang, Q. Wang, Q. Xu, J. Yin, *ChemistrySelect* **8**, e202204944 (2023).
25. J. Lei, Y. Xie, A. Kutana, K. V. Bets, B. I. Yakobson, *J. Am. Chem. Soc.* **144**, 7497–7503 (2022).
26. A. M. van der Zande *et al.*, *Nat. Mater.* **12**, 554–561 (2013).
27. W. Li *et al.*, *Nature* **613**, 274–279 (2023).
28. V. Kranthi Kumar, S. Dhar, T. H. Choudhury, S. A. Shivashankar, S. Raghavan, *Nanoscale* **7**, 7802–7810 (2015).
29. A. Sebastian, R. Pendurthi, T. H. Choudhury, J. M. Redwing, S. Das, *Nat. Commun.* **12**, 693 (2021).
30. Z. Wang *et al.*, *Adv. Mater.* **35**, e2209371 (2023).
31. W. Hong, C. Park, G. W. Shim, S. Y. Yang, S.-Y. Choi, *ACS Appl. Mater. Interfaces* **13**, 50497–50504 (2021).
32. K. Zhang *et al.*, *ACS Appl. Mater. Interfaces* **10**, 40831–40837 (2018).
33. W. Hong, C. Park, G. W. Shim, S. Y. Yang, S.-Y. Choi, *Adv. Electron. Mater.* **8**, 2101325 (2022).

ACKNOWLEDGMENTS

Funding: This work was supported by the National Key R&D Program of China (grant nos. 2022YFB4400100, 2023ZD0120704, and 2023YFF1500500); the National Natural Science Foundation of China (grant nos. T2221003, 62322408, 62204113, U24A20295, 92464303, T2321002, 22033002, 22503062 and 22222302); the Fundamental and Interdisciplinary Disciplines Breakthrough Plan of the Ministry of Education of China (JYB2025XDXM120); the Postdoctoral Fellowship Program and China Postdoctoral Science Foundation (grant nos. BX20250298, BX20240250 2025M780131 and 2025M780510); the Postdoctoral Fellowship Program of CPSF (grant no. GZC20240675); the Natural Science Foundation of Jiangsu Province (grant nos. BK20232001, BK20232024, BK20232012, BK20222007, and BG2024017); the Natural Science Foundation for Young Scholars of Jiangsu Province (grant nos. BK20250530 and BK20251182); the Suzhou Science and Technology Program (ZXL2024359); the Key Laboratory of Advanced Photonic and Electronic Materials; the Collaborative Innovation Center of Solid-State Lighting and Energy-Saving Electronics; and the Big Data Computing Center of SEU and National Supercomputing Center in Tianjin. L.L. and Y.W. acknowledge the support of the Jiangsu Funding Program for Excellent Postdoctoral Talent. T.L. and D.F. acknowledge the support of the Xiaomi Foundation and the Yachen Foundation. X.W. acknowledges support from the New Cornerstone Science Foundation through the XPLORER PRIZE. **Author contributions:** X.W. conceived and supervised the project. L.L. performed the MOCVD growth under the supervision of T.L. with assistance from Y.W., S.M., L.W., W.X., and S.Z. R.D., L.M., and J.W. performed the density functional theory calculations. D.F., F.L., and Y.S. contributed to transistor fabrication, measurements, and data analysis. M.F. and N.Z. performed the AI identification of Domain Detection and Nucleation Quantification. S.W. performed the TEM characterization and data analysis. L.L., Y.W., and S.M. performed XPS, AFM, PL, Raman, and SHG tests. Y.W. performed the mass spectrometry tests. Q.Y., Y.G., and Z.H. performed sample preparation and test of the low-temperature PL. L.L., R.D., T.L., J.W., and X.W. cowrote the paper with input from the other authors. All authors contributed to the discussions. **Competing interests:** A provisional patent has been filed on method and equipment for preparing wafer-scale molybdenum disulfide single-crystal films in China (application no. 202610040297.7; X.W., Y.W, L.L., and T.L., Suzhou Laboratory and Nanjing University). The remaining authors declare no competing interests. **Data, code, and materials availability:** All data and materials synthesis methods are available in the main text or the supplementary materials.

SUPPLEMENTARY MATERIALS

science.org/doi/10.1126/science.aec7259
Materials and Methods; Supplementary Text; Figs. S1 to S18; Tables S1 to S3; References (*34*–*56*); Movies S1 to S4

Submitted 30 September 2025; accepted 11 December 2025

10.1126/science.aec7259

Kinetic acceleration of MoS_2 growth by oxy-metal-organic chemical vapor deposition

Lei Liu, Yushu Wang, Ruikang Dong, Dongxu Fan, Si Meng, Lang Wu, Shengqiang Wu, Wei Xu, Mingwei Feng, Ningmu Zou, Qingyu Yan, Zehua Hu, Fei Lu, Shitong Zhu, Yuan Gao, Liang Ma, Yi Shi, Taotao Li, Jinlan Wang, and Xinran Wang

Science **391** (6784), . DOI: 10.1126/science.aec7259

Editor's summary

Adding oxygen to the mixture of precursors in metal-organic chemical vapor deposition has been shown to accelerate the growth of molybdenum disulfide. Liu *et al*. converted the precursors into high-purity transition-metal oxides and chalcogens, which boosted growth rates and domain sizes by orders of magnitude and prevented carbon contamination. Growth on 15-centimeter miscut sapphire substrates created well-aligned domains and films with average mobilities exceeding 100 square centimeters per volt per second. —Phil Szuromi